technische universität
dortmund

Arbeit zur Erlangung des akademischen Grades
Bachelor of Science

Studies on the properties of non-prompt photons at the ATLAS experiment

Chiara Deponte
geboren in Herdecke

2022

Lehrstuhl für Experimentelle Physik IV
Fakultät Physik
Technische Universität Dortmund

Erstgutachter:	Prof. Dr. Kevin Kröninger
Zweitgutachter:	Dr. Hans Dembinski
Abgabedatum:	15. Juli 2022

Abstract

In this thesis, the properties of non-prompt photons are investigated to contribute to the improvement of the separation of prompt and non-prompt photons at the ATLAS experiment. For this purpose, Monte-Carlo samples simulated with conditions that resemble data-taking in 2017 by the ATLAS detector are used. In that year, data corresponding to an integrated luminosity of $44.39\,\text{fb}^{-1}$ were taken in proton-proton collisions at a centre-of-mass energy of $\sqrt{s} = 13\,\text{TeV}$. Two samples are used for these studies: a dijet sample enriched with non-prompt photons and a γ+jet sample enriched with prompt photons for comparison purposes. The samples are analysed in regard to differences between converted and unconverted photons as well as the impact of the fragmentation fraction $z = p_{\text{T}}^{\text{hadron}}/p_{\text{T}}^{\text{jet}}$ of the leading non-prompt photon on its isolation, its shower shape variables and its probability of passing the tight identification working point. It was determined that this probability increases with a rising fragmentation fraction. A higher fraction also reduces the energy remaining for other particles and thus the average number of particles in the jet, which is why the photon tends to be more isolated. Additionally, the distributions of the shower shape variables of a photon with high z become generally more similar to the distributions of prompt photons.

Kurzfassung

In dieser Arbeit werden die Eigenschaften von nicht-prompten Photonen untersucht, um zur Verbesserung der Trennung von prompten und nicht-prompten Photonen am ATLAS-Experiment beizutragen. Zu diesem Zweck werden Monte-Carlo-Datensätze mit Bedingungen simuliert, die der Datennahme des ATLAS-Detektors im Jahr 2017 ähneln. In dem Jahr wurden Daten, die einer integrierten Luminosität von $44,39\,\text{fb}^{-1}$ entsprechen, in Proton-Proton-Kollisionen bei einer Schwerpunktsenergie von $\sqrt{s} = 13\,\text{TeV}$ aufgenommen. Für diese Studien werden zwei Datensätze verwendet: ein Dijet-Datensatz, der mit nicht-prompten Photonen angereichert ist, und ein γ+jet-Datensatz, der mit prompten Photonen angereichert ist und Vergleichszwecken dient. Die Datenanalyse erfolgt hinsichtlich der Unterschiede zwischen konvertierten und unkonvertierten Photonen sowie der Auswirkungen des Fragmentierungsbruchteils $z = p_{\text{T}}^{\text{hadron}}/p_{\text{T}}^{\text{jet}}$ des führenden nicht-prompten Photons auf seine Isolation, die Form seines Schauers und seine Wahrscheinlichkeit, die Anforderungen des tight-Arbeitspunkts der Photonidentifikation zu erfüllen. Es wurde festgestellt, dass diese Wahrscheinlichkeit mit steigendem Fragmentierungsbruchteil zunimmt. Ein höherer Bruchteil verringert auch die für andere Teilchen verbleibende Energie und damit die durchschnittliche Anzahl der Teilchen im Jet, weshalb das Photon tendenziell isolierter ist. Außerdem werden die Verteilungen der Variablen, die die Form des Schauers eines Photons beschreiben, mit hohem z im Allgemeinen den Verteilungen prompter Photonen ähnlicher.

Contents

1 Introduction

Elementary particles and their interactions via the strong, weak and *electromagnetic* (EM) forces are described by the *Standard Model* (SM) of particle physics. This description agrees well with past and current measurements at collider physics experiments, showing that the SM is a valid foundation for experimental particle physics, even though various problems prove that the model has shortcomings. The predictions of the SM and several *Beyond the Standard Model* (BSM) theories are investigated at the LHC, for example with the ATLAS experiment.

Photons play an essential role in several processes that are used to test the SM or BSM theories, like the production of the Higgs boson in hadronic collisions and the subsequent decay into two photons. Such processes are well suited for testing the SM and probing BSM theories since photons in the final state provide an experimentally clean signature. Nevertheless, these analyses suffer from background consisting of non-prompt photons, meaning reconstructed photons that are neither direct nor fragmentation photons, for example photons from hadron decays. This is why it is important to acquire detailed knowledge about them. This knowledge is necessary so that they can be well separated from the prompt photons.

In this thesis, the properties of non-prompt photons are investigated to contribute to improving this separation at the ATLAS experiment. For this, *Monte-Carlo* (MC) samples are used whose conditions are similar to the data-taking of the ATLAS collaboration in 2017. The tight identification *Working Point* (WP) for photons at ATLAS is based on cuts on various *Shower Shape Variable*s (SSVs) and the isolation WPs apply cuts on the isolation variables to suppress background from non-prompt photons. It should be noted that the criteria of the tight WP are parametrised based on the kinematics of the photon candidate and differ between converted and unconverted photons.

Since converted photons are electron-positron pairs they differ from unconverted photons and it is of interest whether the conversion status influences the properties of non-prompt photons and to compare differential distributions of the ratio of converted and unconverted photons for both prompt and non-prompt photons. Furthermore, the impact of the fragmentation fraction on the properties of the reconstructed photon, e.g. the shower shape variables, is discussed. Moreover, the relationship of the isolation variables of non-prompt photons with the identification status, as well as their correlation with selected kinematical variables of the photon are analysed. Also, the influence of the flavour of the parton initiating the closest jet of the leading photon is investigated. These studies close with a final interpretation of the results.

2 Photons in the Standard Model

In this chapter, a brief overview of the SM of particle physics with special regard to the role of the photon is given. The theoretical introduction is provided in Section 2.1 while Section 2.2 covers the relevance of photons for collider physics in more detail.

2.1 Summary of the Standard Model

At the moment, the SM is the most successful theory of experimental particle physics. It is in excellent agreement with measurements and the data recorded so far. Yet there have been no generally accepted measurements with a tension of 5σ to the SM prediction, which is the conventional limit in particle physics to claim a discovery. The SM is a quantum field theory which describes the interactions of elementary particles via the strong, weak and EM forces [1–4]. The characterised particles are shown in Figure 2.1.

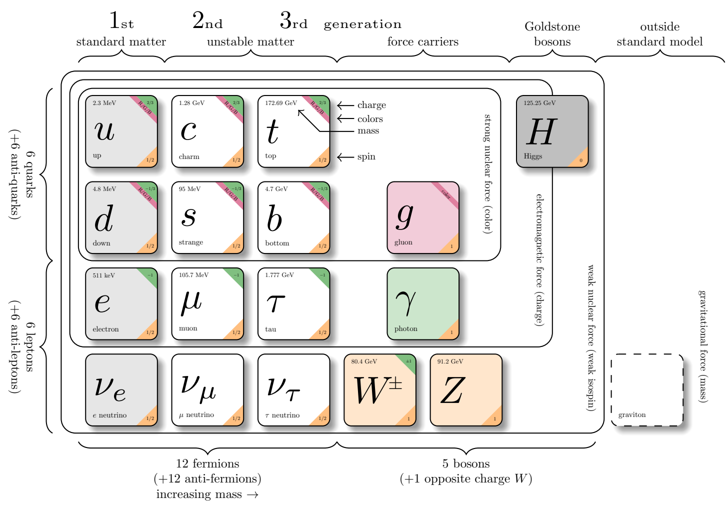

Figure 2.1: The properties and interactions of the particles described by the SM adapted from [5].

There are two types of particles, fermions with a spin of $s = \frac{1}{2}$ and bosons with an integer spin. The gauge bosons with a spin of $s = 1$ mediate the three fundamental forces, while the only other boson, the Higgs boson, has a spin of $s = 0$.

The fermions are divided into quarks, which interact via all three forces, and leptons, which do not interact strongly. For each fermion, there is an anti-particle with inverted additive quantum numbers, such as the charge. Quarks and leptons come in three generations with increasing mass but otherwise similar properties. The leptons are subdivided into the electrically uncharged neutrinos, which only interact via the weak force, and electrons, muons and tau leptons with a charge of $q = -e$, which interact via the EM and the weak force. Out of the quarks, three have a positive charge of $q = \frac{2}{3}e$ (up-type) and three have a negative charge of $q = -\frac{1}{3}e$ (down-type).

Quantum Chromodynamics (QCD) is a non-abelian gauge theory, which describes the strong force. This force is mediated by gluons, which couple to colour charge, which every strong interacting particle carries. There are eight distinct gluons, which have different colour-anticolour combinations. Self-coupling between gluons is allowed by the strong force. For high energies or small distances, the strong coupling constant α_s declines thus the interactions between quarks and gluons become weaker. Therefore, they behave as if they were almost non-interacting. This is called asymptotic freedom. With decreasing energy or increasing distance they cannot exist in isolation but form colourless bound states for example protons and neutrons. This is referred to as hadronisation. Because of this confinement quarks are not directly observable. Very high energetic quarks and gluons fragment into multiple hadrons forming a narrow cone called a jet.

The weak force changes the flavour[1] of the interacting particles. It is mediated by the electrically uncharged Z boson and the charged $\mathrm{W}^\pm$ bosons. In contrast to the massless gluons, $\mathrm{W}^\pm$ and Z bosons are massive. The transition of, for example, electrons into antielectron neutrinos takes place via the charged current ($\mathrm{W}^\pm$ bosons). The neutral current (Z boson) couples to same flavour fermions.

The Higgs field [6–11] solved the problem of why the $\mathrm{W}^\pm$ and Z bosons are massive in contrast to the other gauge bosons. Thus, it was possible to unify the EM and weak interactions into the electroweak force. The Higgs field is a scalar self-interacting field with a non-vanishing vacuum expectation value. It breaks the electroweak symmetry without breaking the gauge symmetry of the Lagrangian. By interacting with a particle, it gives it mass. Accordingly, massless particles do not interact with the field. Since the Higgs field cannot be measured directly, it can only be detected by the Higgs boson, which is defined as a wave in the Higgs field.

Contrary to QCD, *Quantum Electrodynamics* (QED) is an abelian gauge theory, which means that photons are not able to couple to themselves. Since the photon is massless, the Higgs boson does not directly interact with it. For that reason, photons and QED can often be analysed separately without considering Z and $\mathrm{W}^\pm$ bosons.

$$\mathcal{L}_\mathrm{QED} = \overline{\psi}(i\not{D} - m) - \frac{1}{4}F_{\mu\nu}F^{\mu\nu} \tag{2.1}$$

is the QED Lagrangian with a charged Dirac field ψ associated with a fermion f with

[1] Flavour is a synonym for the particle type of fermions.

mass m and the photon vector field A_μ. The asymmetric electric field strength tensor in the second term is given by $F_{\mu\nu} = \partial_\mu A_\nu - \partial_\nu A_\mu$ and the covariant derivative is defined as $D_\mu = \partial_\mu + ieA_\mu$. From the requirement of gauge invariance follows a coupling of the described electron and photon. Furthermore, equation 2.1 is parity, charge and time invariant. A coupling of the electron or photon to itself is not possible. A mass term for the photon is also not possible.

2.2 Relevance of Photons for Collider Physics Experiments

The goal of collider physics is a better insight and description of elementary particles and their bound states as well as the fundamental forces. For this purpose, theories such as the SM are tested for their validity. For the measurements, there are fixed framework conditions such as the detector, the centre-of-mass energy and the type of particle used, in the case of the LHC, protons and heavy ions. The SM is a valid foundation for experimental particle physics, even though various problems indicate that the model has shortcomings. For instance gravity [12], the asymmetry of the quantities of matter and antimatter in the universe [13] and dark matter [14] are neither part of nor being explained in the SM. Photons are suitable for testing aspects of the SM since QED is a comparatively well understood theory and photons in the final state provide an experimentally clean signature. Furthermore, photons are part of important processes such as the decay of the Higgs boson into two photons, but this is not in the scope of the thesis since it is a study on non-prompt photons. Since non-prompt photons form the background of such a measurement, it is very important to understand them precisely so that they can be well separated from prompt photons.

The diagrams in Figure 2.2 depict photon production, the first three describing the main topologies from which prompt and non-prompt photons can be extracted.

In collider physics, reconstructed photons are classified into prompt and non-prompt photons. Prompt photons are subdivided into direct and fragmentation photons. Direct photons are produced during hard-scattering processes (see Figure 2.2a). When energetic quarks or gluons from the hard-scattering process hadronise, colourless hadronic bound states are created as explained in Section 2.1. Instead of the production of hadrons, fragmentation can also give rise to a photon (see Figure 2.2b) [15,16]. The probability density that a parton i produces a hadron h with the momentum ratio $x = p_\mathrm{T}^\mathrm{hadron}/p_\mathrm{T}^\mathrm{parton}$ is described by the fragmentation function $D_i^h(x^2, \mu^2)$ [17]. Since the transverse momentum of the parton is not known, the equivalent experimental variable $z = p_\mathrm{T}^\mathrm{hadron}/p_\mathrm{T}^\mathrm{jet}$ is being used. For this thesis, the most relevant fragmentation is that of a quark or gluon into a π_0 meson which decays into two photons (see Figure 2.2c) as it is the most common particle with this decay. Since π_0 mesons are generally produced with a transverse momentum that is significantly larger than their mass, they have very large Lorentz factors. Due to this, the photons generated have a very small opening angle and can be misreconstructed

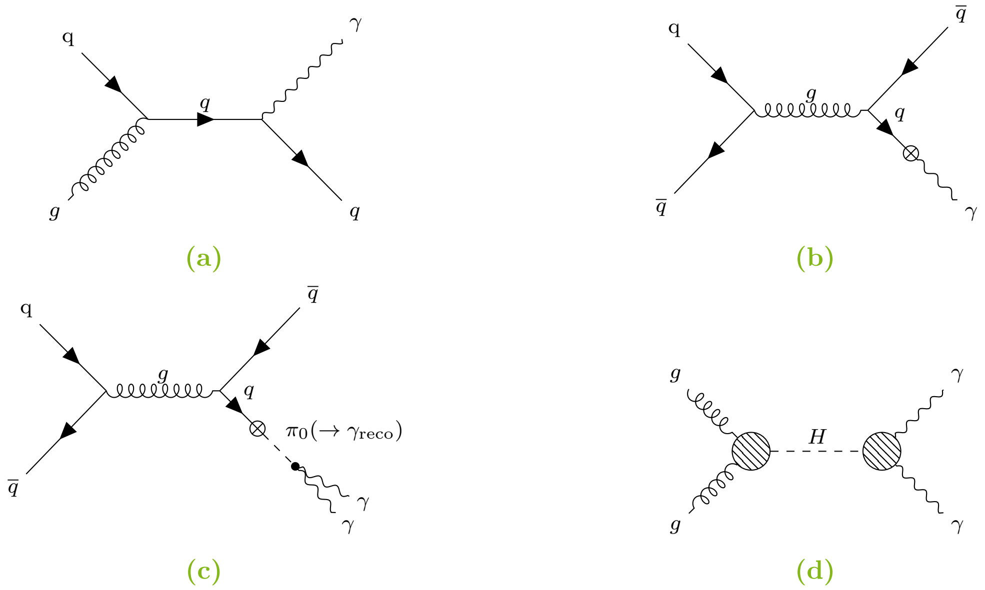

Figure 2.2: Diagrams showing the production of photons in various topologies in hadron-hadron collisions. Diagram (a) (γ+jet) shows the production of a direct photon alongside a quark. (b) depicts the production of a quark-antiquark pair with subsequent fragmentation into a photon. (c) displays a dijet event in which a quark fragments into a π_0 meson decaying into two photons which is misreconstructed as a photon. In (d) is the production of a Higgs boson with a subsequent decay in the diphoton channel illustrated. For simplicity, the loops of the effective coupling were denoted by circles.

as a single photon. These mesons form the main contribution to the class of non-prompt photons. Non-prompt photons also originate from other hadron decays for example the decay of the η meson into two photons. Furthermore, it is possible that electrons are misreconstructed as photons. The reconstruction at the ATLAS experiment is further discussed in Section 3.2.

The photon is a very important particle for the study of the Higgs boson, as the decay of the Higgs boson into two photons is one of the cleanest decay channels. It is one of the decays that led to the discovery of the Higgs boson by the ATLAS [18] and the CMS [19] experiment in 2012, which is shown in Figure 2.2d. For simplicity, the loops of the effective coupling between the gluons and photons with the Higgs boson were denoted by circles.

Photons are also part of various processes that are used to test properties of the SM, such as the fiducial cross-section for electroweak production [20,21], perturbative QCD [22,23] or the coupling of top quarks to photons [24,25]. But equally, there are also several processes with photons that are predicted by BSM theories [26,27]. Thus, photons are not only relevant for the testing of the SM, but also for BSM research.

3 The ATLAS experiment at the Large Hadron Collider

The *Conseil Européen pour la Recherche Nucléaire* (CERN) is a large international organisation for research in particle physics located in France and Switzerland. Operating the *Large Hadron Collider* (LHC) [28] and analysing data taken there is one of the focuses of the CERN research program. The particle accelerator is placed in a circular tunnel with a circumference of 27 km and has an ultrahigh vacuum in the tubes. It is the world's largest and most powerful collider and is used to collide two high energy particle beams composed of protons or heavy ions. Four main experiments are located around the ring, namely ATLAS [29], CMS [30], LHCb [31] and ALICE [32]. ATLAS and CMS are general-purpose detectors with similar overall physics goals but with different subdetector designs. LHCb is a forward detector, which is used to study bottom-quarks and the CP violation, among other things. ALICE is aimed at heavy-ion physics.

In the period of data collection from 2015 until 2018 proton-proton collisions occured at a centre-of-mass energy of $\sqrt{s} = 13\,\text{TeV}$. In this period ATLAS has taken data corresponding to an integrated luminosity of $139\,\text{fb}^{-1}$. The integrated luminosity of ATLAS in 2017 was $44.39\,\text{fb}^{-1}$ [33], significantly greater than in previous years and accompanied by substantially more pile-up. Pile-up is the background resulting from additional proton-proton collisions that occur in the same bunch-crossing as the collision under consideration or shortly before or after it.

From 2022 until the end of 2025, the LHC will run at a centre-of-mass energy of $\sqrt{s} = 13.6\,\text{TeV}$ [34].

3.1 The ATLAS Detector

The ATLAS detector has a cylindrical shape and is forward-backward symmetric. For its describtion a right-handed coordinate system is used, which has its origin in the nominal interaction point. The z-axis lies along the beam pipe, the x-axis points into the middle of the ring and the y-axis points upwards. In the transverse plane spanned by the x- and y-axis, polar coordinates r and ϕ are used. The plane is used for the calculation of the transverse momentum $p_\text{T} = p_x^2 + p_y^2 = |\vec{p}| \sin\theta = |\vec{p}|/\cosh\eta$ and the transverse energy $E_\text{T} = E/\cosh\eta$. The pseudorapidity η is calculated through the polar angle between the beam pipe and the particle via $\eta = -\ln\tan\theta/2$. For angular distances between objects, $\Delta R = \sqrt{(\Delta\eta)^2 + (\Delta\phi)^2}$ is used.

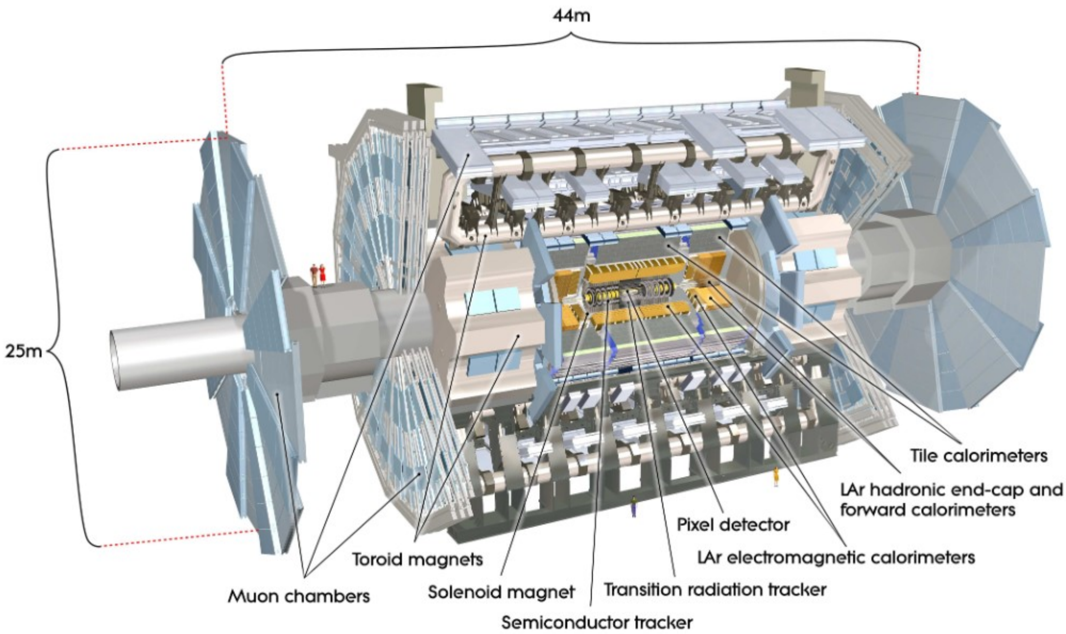

Figure 3.1: Cut-away view of the ATLAS detector with its main components [29].

The main subcomponents of the ATLAS detector are shown in Figure 3.1. It is composed of an *Inner Detector* (InDet), an *Electromagnetic Calorimeter* (ECAL), a *Hadronic Calorimeter* (HCAL) and a *Muon spectrometer* (MS). Each subdetector is divided into a barrel section and two end-cap sections. The barrel section is the central region of the detector covering roughly $|\eta| < 1.5$ while the end-cap section covers a pseudorapidity region closer to the beam pipe (see Figure 3.1).

The InDet is used to track charged particles covering a range of $|\eta| < 2.5$ and made of concentric cylinders around the beam axis. It consists of the high-resolution semiconductor pixel tracker and the *Silicon Microstrip Tracker* (SCT) in the inner part and the *Transition Radiation Tracker* (TRT) made of gas-filled straw tubes in the outer part. The TRT covers only a range up to $|\eta| = 2$ and measures radiation emitted during the transition of a particle into another medium. The intensity of the radiation depends on the Lorentz factor of the particle, providing information to discriminate particles with different masses, such as electrons and pions. The TRT does not provide as accurate measurements as the SCT, but takes a considerably larger number of measurements and measures over a longer track length. The InDet is surrounded by a thin superconducting solenoid which creates a 2 T strong magnetic field. It is used to measure the momentum and charge of passing particles. The charge is calculated from the curvature of the particle's path in the magnetic field.

The ECAL covers a pseudorapidity range up to $|\eta| < 3.2$. It is a high granularity sampling calorimeter made of *liquid-argon* (LAr) as the active material and lead as the absorber. The total thickness is greater than 22 *radiation length* (X_0) in the barrel and greater than 24 X_0 in the end-cap. The X_0 of a material is the average length to reduce the energy of an electron through bremsstrahlung by the factor $1/e \approx 37\,\%$. The ECAL has an accordion geometry providing ϕ symmetry and is segmented into three sections in depth in lateral direction. The first layer is called the strip layer and is the most granular layer. It is used to identify double-peaked structures, for example two collimated photons from the decay of π_0 mesons. They have to be discriminated from prompt photons to increase the purity in analyses with photons in the final state.

The HCAL directly encloses the ECAL. For $|\eta| < 1.7$, it is a sampling calorimeter using steel as the absorber and scintillating tiles as the active material. Similar to the ECAL, it is segmented into three layers in depth. For $1.5 < |\eta| < 3.2$ it consists of two independent wheels made of copper with LAr gaps.

The LAr forward calorimeter extends up to $3.1 < |\eta| < 4.9$. The active material is LAr and the absorber is either copper or tungsten.

To provide a magnetic field to measure the momenta of the muons, three large superconducting toroids are placed between the calorimeter and the system giving ATLAS (A Toroidal LHC ApparatuS) its name. One is placed in the barrel and one in each endcap.

The muon system covers the range of $|\eta| < 2.7$ and is used to measure particles that pass through the HCAL, mainly muons. It measures their momentum via their curvature in the magnetic field, which is provided by three air-core torodial magnets, combining tracking and fast trigger chambers.

3.2 Electromagnetic Objects and Jets at the ATLAS Experiment

For this work, mainly photons are relevant, but also electrons. The signature of an electron is a track pointing towards the cluster associated with the shower, which the electron created in the ECAL. Due to the material in front of the calorimeters, some of the photons convert into electron-positron pairs[1]. In the central region, about 20% of the photons convert, while for $\eta = 2.3$ the conversion fraction is about 65% [35]. Since photons are electrically neutral, they leave no track in the InDet, only a shower in the ECAL. As converted photons convert at some point into electrons, there is a conversion vertex that originates outside the beam pipe. Since it is possible that an electron was not detected or reconstructed, this vertex is composed of one or two tracks.

The signatures of electrons and unconverted as well as converted photons are visualised in Figure 3.2. Depending on the reconstruction of tracks and conversion vertices close to EM objects, these three categories can sometimes be mixed up.

[1] In the following, both electrons and positrons will be referred to as electrons for simplicity.

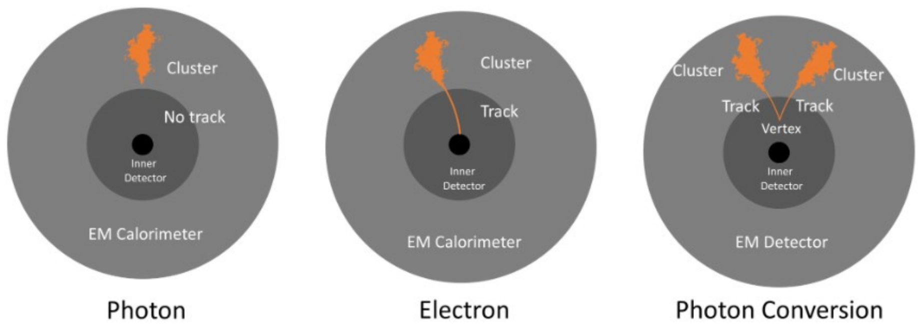

Figure 3.2: The signatures of photons, electrons and photon conversions in the ATLAS detector [36].

Since tracking is essential for distinguishing electrons and photons, no reconstructed particles from the forward calorimeter are used in this thesis, as no tracking is available there.

As electrons and photons create similar showers, the reconstruction proceeds in a unified approach [35,37]. For the reconstruction of EM objects, proto clusters are built first. They are seeded by energetic cells in the second layer of the ECAL. All neighbouring cells with a significance[2] of at least 4 and then at least 2 are added to the seeds. If two proto clusters contain the same cell they are merged. The opposite is the case for clusters with two local maxima, which are divided into independent clusters. Afterwards, super clusters are formed from a proto cluster and so-called satellite clusters. These satellite clusters arise for example from emitted bremsstrahlung.

The tracks, conversion vertices and the clusters are created separately and matched afterwards. Following that, the electron and photon objects used in analysis are reconstructed. For this process only the energy measured in the ECAL is used.

Reconstructed EM objects can be ambigous, for example one object could be reconstructed as a converted photon and an electron. To resolve such ambiguities the method described in Reference [38] is used.

In order to seperate prompt photons from non-prompt photons, photon candidates are required to fulfill criteria of variables that offer discriminative power. The used variables describing the properties of the showers are depicted in Figure 3.3. The loose identification WP is $|\eta|$-, but not p_{T}-dependent and uses, contrary to the tight WP, only some of the displayed SSVs. However, the tight WP is both p_{T}- and $|\eta|$-dependent.

In addition, the track and calorimeter isolation is used to define different WPs, with given signal and background efficiencies. The isolation variable $p_{\mathrm{T}}^{\mathrm{cone20}}$ is defined as the sum of the transverse momenta of all tracks surviving basic quality criteria in the radius

[2]The significance is defined as $|\zeta_{\mathrm{cell}}^{\mathrm{EM}}| = \frac{E_{\mathrm{cell}}^{\mathrm{EM}}}{\sigma_{\mathrm{noise,cell}}^{\mathrm{EM}}}$ [35].

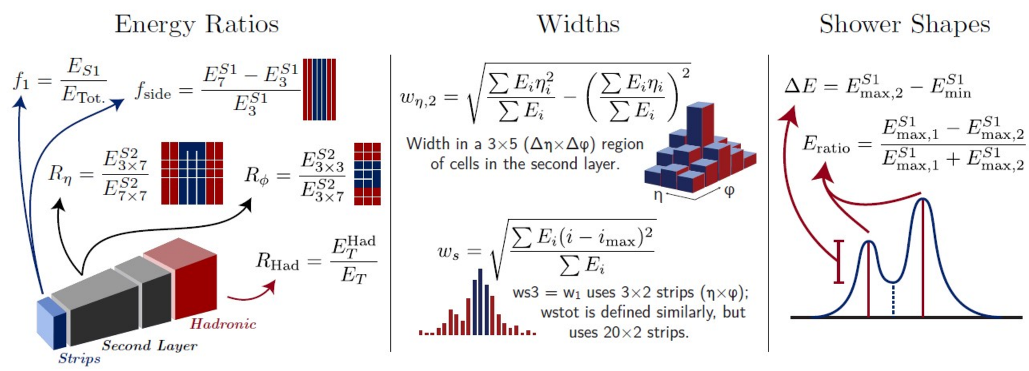

Figure 3.3: Schematic of the different SSVs [39].

$\Delta R = 0.2$ around the photon [35]. The contribution of the object under consideration is not taken into account. Similarly, $E_{\mathrm{T}}^{\mathrm{cone20}}$ or $E_{\mathrm{T}}^{\mathrm{cone40}}$ refer to the energy deposition in the radius $\Delta R = 0.2$ or $\Delta R = 0.4$ around the photon, removing the cluster associated with the considered object. For the calculation of $E_{\mathrm{T}}^{\mathrm{cone}}$, the energy from a fixed cell area around the barycentre of the cluster is subtracted from the energy measured [35]. Therefore, an additional correction is necessary, but this may cause $E_{\mathrm{T}}^{\mathrm{cone}}$ to take on negative values.

Jets are reconstructed with the anti-k_t algorithm [40] using a radius parameter of $R = 0.4$ and the FastJet package [41]. Their constituents are recovered with the particle-flow algorithm [42], combining accurate spatial information and momentum measurement from the InDet for charged particles and energy measurement from clusters in the calorimeters for charged and neutral particles. After the calibration the reconstructed jets are required to have a momentum of $p_{\mathrm{T}} > 20\,\mathrm{GeV}$ and a pseudorapidity $|\eta| < 4.5$. Jets originating from pile-up are suppressed via Jet Vertex Tagging (JVT) [43].

3.3 Relevant Processes and Simulated Datasets

For the studies presented in this thesis two different MC samples were used. They were simulated with Pythia 8 [44] and processed with the ATLAS software framework [45] as well as a complete ATLAS detector simulation with Geant 4 [46]. The samples correspond to the data taking conditions of 2017, meaning a centre-of-mass energy of 13 TeV and more pile-up than in the years before. The mean number of interactions per crossing increased to $\langle\mu\rangle = 37.8$ in 2017 compared to $\langle\mu\rangle = 13.4$ and $\langle\mu\rangle = 25.1$ in 2015 and 2016, respectively [47]. For this analysis, truth information about reconstructed objects based on geometrical matching and internal generator information is available.

Simulated events are assigned a weight consisting of the following factors: The MC generator weight, a pile-up weight to reproduce the distribution of $\langle\mu\rangle$ measured in data, the cross section, the integrated luminosity of the data and a correction factor for the modelling of the z-position of the primary vertex. Only the uncertainties due to the limited MC statistics are taken into account.

There are two possible definitions for the pseudorapidity: In the first definition, the pseudorapidity of the barycentre of the cluster is measured in the second layer of the ECAL. The second possibility is to extrapolate a straight track connecting the collision point to the centre of the cluster. The resulting values of these definitions are not equal. In this thesis, only the first definition is used for the pseudorapidity.

The photons in the first sample are to a large extent non-prompt because the fragmentation photons were removed. It is a dijet sample containing jets with a generator-level p_T between 20 and 160 GeV. For this sample, no overlap removal was performed meaning that jets near reconstructed photons are kept. The reason for this is that a large proportion of the photons under consideration originate from hadron decays inside jets. Therefore, the properties of these jets are relevant.

Since background photons are to be investigated in the studies, only non-truth matched photons are used. Furthermore, the events used must have at least one jet and a maximum angular distance of $\Delta R = 0.6$ between the photon and the closest jet. Due to lack of precision, no events from the transition region $1.37 < |\eta| < 1.52$ between barrel and endcap region are used. After the selection, 8306578 of the original 9741080 events are left.

The photons in the second sample are to a large extent prompt photons. This includes direct photons from γ+jet events and fragmentation photons. The fragmentation photons are obtained from dijet events, in which one of the quarks or gluons fragments into a photon. After requiring the leading photon to be truth matched and to have a transverse momentum in the range of $20\,\text{GeV} \leq p_{\text{T}}^{\gamma} \leq 150\,\text{GeV}$, 996967 of the 1000000 events remain. The cut on the momentum of the photons ensures the comparability of the two samples. As in the first sample, no events in the transition region are used.

With the increase of the centre-of-mass energy of the LHC to 13.6 TeV, the kinematic quantities of reconstructed photons change compared to the conditions on which the samples are based. In addition, there will be a little more pile-up. However, since there was already comparatively much pile-up in 2017 and the centre-of-mass energy was not increased substantially, the results of this thesis should also be applicable for data from the new data-taking period. Furthermore, it is not expected that the photon reconstruction algorithms will be changed significantly in this period. Since the subsequently planned increases in luminosity at the LHC will significantly increase the pile-up rate, these studies will then only be applicable to a limited extent or not at all and would have to be repeated with new samples.

The increasing amount of pile-up particularly concerns the cuts on the SSV and the calculation of the isolation variables. This is being studied in detail by ATLAS [48].

4 Studies of the Properties of Non-Prompt Photons

As described in Section 2.2, many interesting processes suffer from background contributions of non-prompt photons. Therefore, it is necessary to have detailed knowledge about their properties. Hence, in the following sections, dijet and γ+jet events, generated as described in Section 3.3, will be analysed to identify properties to distinguish non-prompt photons from prompt photons. In Section 4.1, the differences between unconverted and converted photons are studied as a function of the photon p_{T} and η and those differences are compared between prompt and non-prompt photons. In Section 4.2 the impact of the fragmentation fraction $z = p_{\mathrm{T}}^{\mathrm{hadron}}/p_{\mathrm{T}}^{\mathrm{jet}}$ on the properties of the reconstructed photon is discussed as a large fraction of the non-prompt photons originates from decays of neutral pions. Section 4.3 deals with the relationship of the isolation variables of non-prompt photons and the identification WPs, as well as their correlation with selected kinematic variables of the photon. The dependence of the SSVs on the fragmentation function as well as the originating parton of the closest jet [1] is analysed in Section 4.4. A summary and evaluation of the results are given in Section 4.5.

4.1 Conversion Rate

Since converted and unconverted photons exhibit differences, the influence of different variables on the conversion status is investigated. It is uncertain as what collimated photons are reconstructed when one or both photons convert. Furthermore, it is unclear whether unconverted photons from neutral meson decays with a larger opening angle are incorrectly reconstructed as one converted photon, since this would require extended studies. Therefore, only general trends and observations are noted in this chapter.

In Figure 4.1, distributions for the fraction of converted photons in dependence on the pseudorapidity η [2] can be seen. In Figure 4.1a this is shown for all prompt and non-prompt photons and in Figure 4.1b only for photons passing the tight identification WP. In both figures, non-prompt photons have a significantly larger fraction of converted photons than prompt photons. This is to be expected since the purity of the reconstructed photons is less for converted photons [37]. Furthermore, this effect may

[1] In the following, a jet always means the jet that has the smallest angular distance to the leading photon of the event.

[2] Considering the geometry of the detector and the calorimeter layout, the pseudorapidity binning is given by [0.0, 0.6, 0.8, 1.15, 1.37] and [1.52, 1.81, 2.01, 2.37].

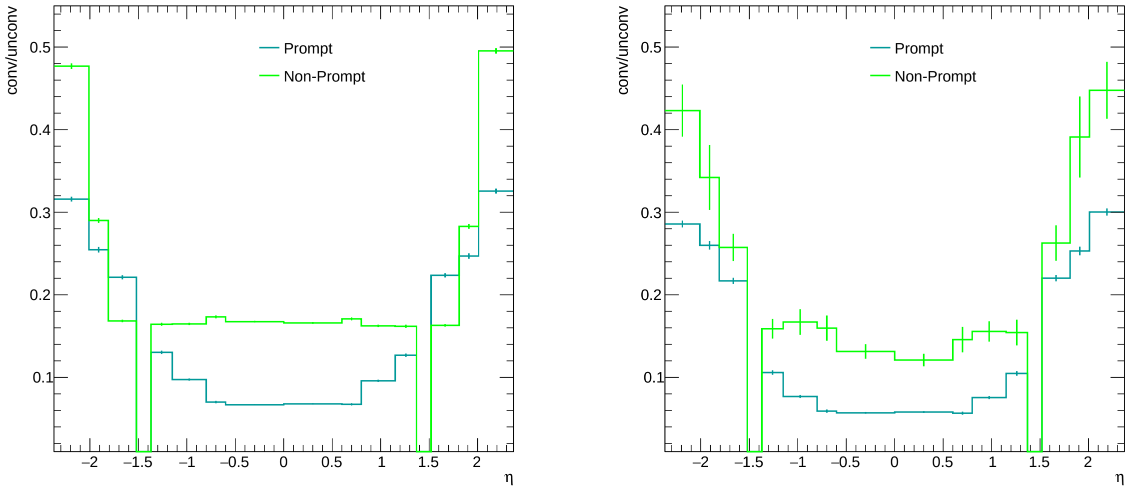

Figure 4.1: The ratio of the numbers of converted and unconverted photons in dependence of the pseudorapidity η for all prompt and non-prompt photons (a) and (b) only for those passing the tight identification WP.

have been amplified in the left figure by the false reconstruction of collimated photons with a larger opening angle as a converted photon. Comparing prompt and non prompt photons passing the tight identification WP it can be seen, that the distributions are more similar than those in 4.1a. This is also to be expected since only signal-like photons with shower shapes resembling prompt photons pass the tight identification criteria. The observation that all fractions increase with η can be explained as the amount of detector material in front of the calorimeter increases for higher pseudorapidities and thus also the conversion probability. The difference between the distributions of all non-prompt photons and those passing the tight identification WP may indicate that the conversion fraction of non-prompt photons is slightly influenced by the requirements of the tight identifcation WP on the SSVs.

In Figure 4.2a, one can see the transverse momentum of the leading photon for unconverted and converted non-prompt photons. It can be observed that converted non-prompt photons are softer than unconverted photons. This was not to be expected since the probability that a prompt photon converts increases logarithmically with its energy [49]. One factor could be the decreasing opening angle of collimated photons for increasing momenta because this presumably raises the probability that they are reconstructed as one unconverted photon.

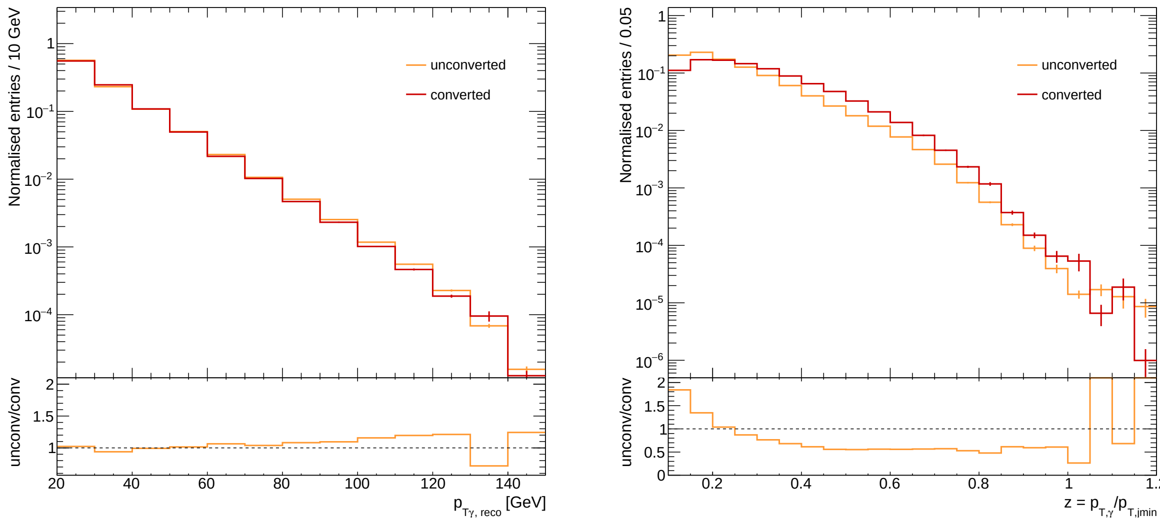

(a)

(b)

Figure 4.2: Figure (a) shows the transverse momentum distributions and (b) the ratio z of the transverse momenta of the leading photon and the closest jet for unconverted and converted non-prompt photons. All histograms are normalised to unit area.

In the figure to the right, the ratio z of the transverse momenta of the leading photon and the closest jet for unconverted and converted non-prompt photons is plotted. Here, exactly the opposite trend can be seen: The probability that a non-prompt photon is reconstructed as converted increases for higher z. It was not to be expected that z and p_T have diffferent trends since they are correlated (see Figure 4.6a).

To investigate these matters further, more information about the photons, such as the conversion radius or the spatial extent of the cluster in the calorimeter, and a much deeper examination of the photon reconstruction algorithms would be necessary. In addition, truth information about the conversion status would be beneficial as the physical mechanisms of photon conversion are more intricate for non-prompt photons from meson decays. However, this is out of the scope of this thesis.

4.2 Fragmentation Fraction

As mentioned before, the opening angle of collimated photons from π_0 meson decays decreases on average for an increasing ratio $z = p_T^{\mathrm{hadron}}/p_T^{\mathrm{jet}}$. Therefore it is important to understand the dependence of the photon identification criteria on the fragmentation fraction.

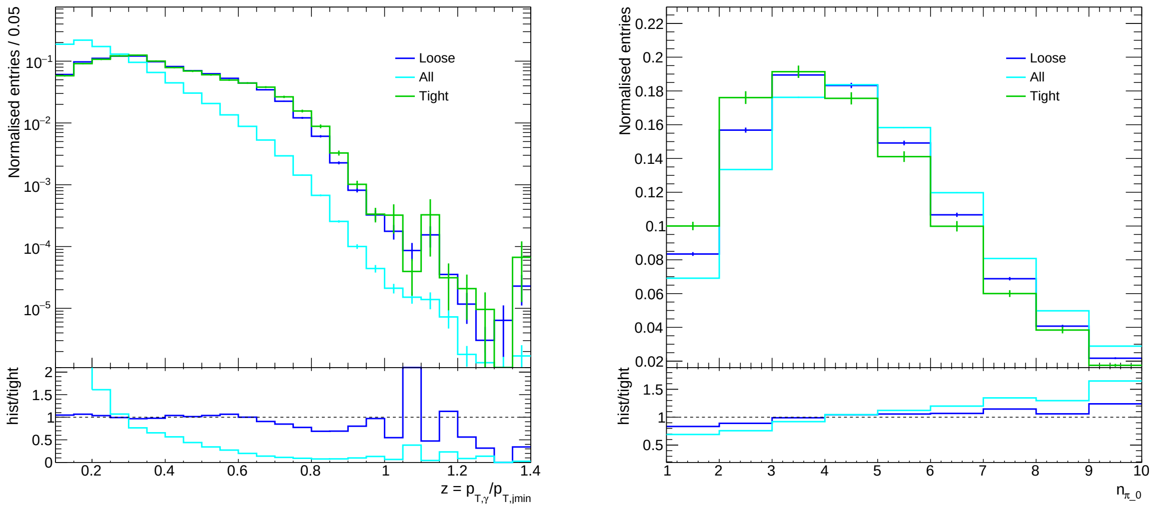

(a) (b)

Figure 4.3: Figure (a) depicts the fragmentation frction of the reconstructed photon and (b) the number of π_0 mesons in the closest jet for all non-prompt photons and those passing the loose or tight identification WP, respectively. All histograms are normalised to unit area.

In Figure 4.3 the ratio z and the number of π_0 mesons in the closest jet for all non-prompt photons and those passing the loose or tight identification WP are shown, respectively. On the left-hand side one can see that tight photons tend to have greater z. This can be explained by the fact that collimated photons from decays of neutral pions with high momenta have small opening angles. This is because showers of collimated photons overlap more for small opening angles, which is why their signatures are more similar to those of single prompt photons (see Section 2.2). π_0 mesons can only reach such high momenta if they receive a large fraction of the momentum of the jet in the fragmentation process. This is much more likely for jets with lower particle multiplicites. This relationship can also be seen in Figure 4.3b, where it is recognisable that the closest jet tends to contain fewer π_0 mesons when considering tight photons.

4.3 Isolation Variables

Section 4.2 motivates why the fragmentation fraction is related to the isolation of non-prompt photons due to the number of particles in the closest jet. This relationship is examined in more detail below. Figure 4.4a depicts the distribution of the isolation variable $p_{\mathrm{T}}^{\mathrm{cone20}}$ for all non-prompt photons and those passing the loose or tight identification WP, respectively. In Figure 4.4b the same is shown for $E_{\mathrm{T}}^{\mathrm{cone20}}$. As can be seen in the

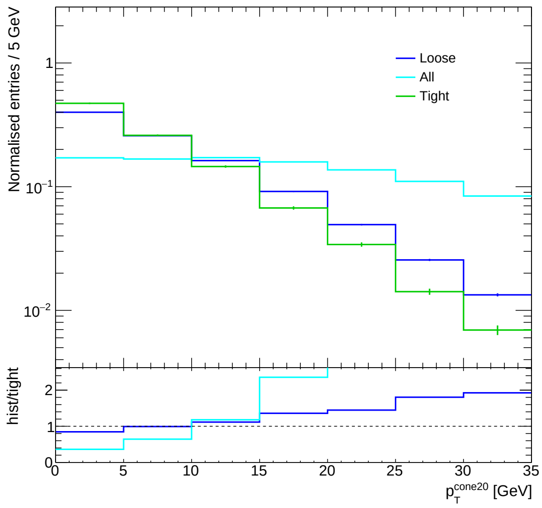

(a)

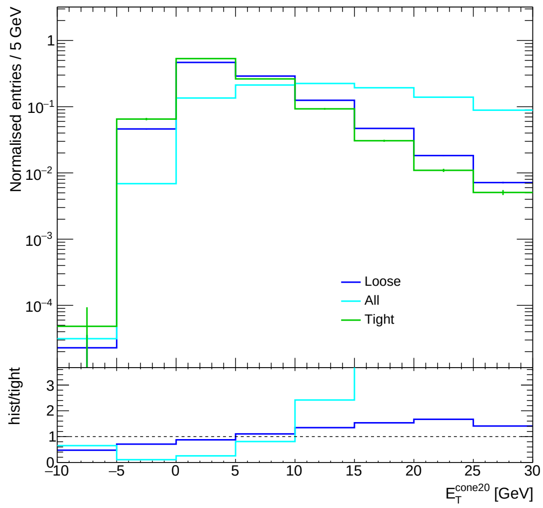

(b)

Figure 4.4: Figures (a) and (b) display normalised distributions of the isolation variables $p_{\mathrm{T}}^{\mathrm{cone20}}$ (a) and $E_{\mathrm{T}}^{\mathrm{cone20}}$ (b) for loose, tight, and all non-prompt photons.

figures, the isolation variables tend to have lower values for tight photons, which means that there are less tracks and less energy depositions in a cone around the particle. This is consistent with the fact that the nearest jet tends to contain fewer neutral pions when it contains a non-prompt photon, which passes the tight identification WP. Similar lower multiplicities are expected for other types of hadrons. This is expected because a higher fragmentation fraction leads to fewer and less energetic particles in the jet. Thus, a direct relationship between isolation and identification variables on the one hand and the fragmentation fraction on the other hand is established.

In Figure 4.5, the number of tracks in a cone with a radius of $\Delta R = 0.6$ around the photon candidate and π_0 mesons in the closest jet is given for loose, tight, and all non-prompt photons in Figure 4.5a and for different z-intervals in Figure 4.5b. The used tracks pass some basic loose quality criteria. They can be used to review the hypothesis that the number of particles in a jet and the momentum ratio z or the identification of photons from a π_0 meson decay are linked, respectively. For these distributions, no criteria to reduce tracks from pile-up interactions are applied since only relative differences are relevant and the average number of these tracks should be similar between the different categories of non-prompt photons. It is evident that jets with tight photons tend to have fewer particles, which confirms the statement made earlier. In the figure on the left, it can be seen that the average number of particles in a jet decreases with tighter requirements on the SSVs. Thus, the similarity of the signatures of non-prompt and prompt photons

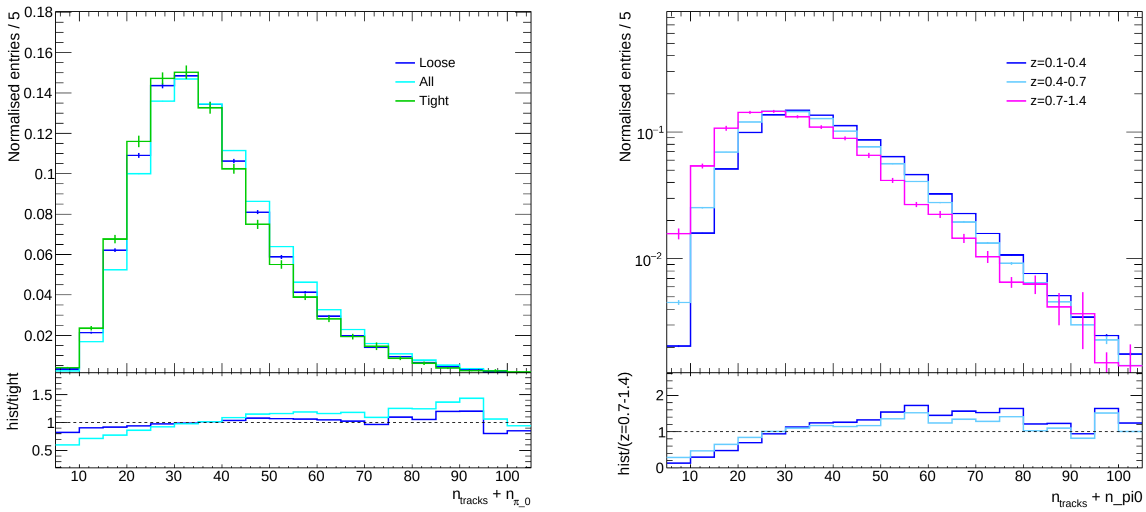

(a) (b)

Figure 4.5: Figure (a) shows the number of π_0 mesons and tracks passing some basic loose quality criteria in the closest jet for loose, tight, and all non-prompt photons and (b) for different z-intervals. The histograms are normalised to unit area.

is inversely correlated to the number of particles in the closest jet. As expected, the distribution of non-prompt photons passing the loose identification point lies between the distributions of those passing the tight identification point and of all non-prompt photons.

The linear correlation between the kinematics of the photon and its isolation variables can be assessed with the Pearson correlation matrix in Figure 4.6a. The non-linear correlation can be found in the Spearman correlation matrix in the Appendix A.1. Since the fragmentation fraction z contains the transverse momentum of the photon in the numerator, a certain degree of correlation is expected and is confirmed in the matrix, validating the matrix' calculation. The isolation variables and z are negatively correlated, which is sensible as for a high z there is less momentum and therefore energy left for all other particles in the jet. The correlation of the isolation variables with each other is also not surprising since an increase in energy depositions around the photon candidate is also linked to more and also more energetic tracks around it. The two-dimensional plane of $E_{\mathrm{T}}^{\mathrm{cone20}}$ in dependence of $p_{\mathrm{T}}^{\mathrm{cone20}}$ is shown in Figure 4.6b. Here, a linear correlation between the variables with scattering around the main diagonal is visible. One reason for this scattering are the fluctuations in the number of electrically neutral and charged particles. In addition, $E_{\mathrm{T}}^{\mathrm{cone20}}$ is reduced more by pile-up subtractions than $p_{\mathrm{T}}^{\mathrm{cone20}}$. Furthermore, detector effects and a limited resolution cause that the jets' energy can

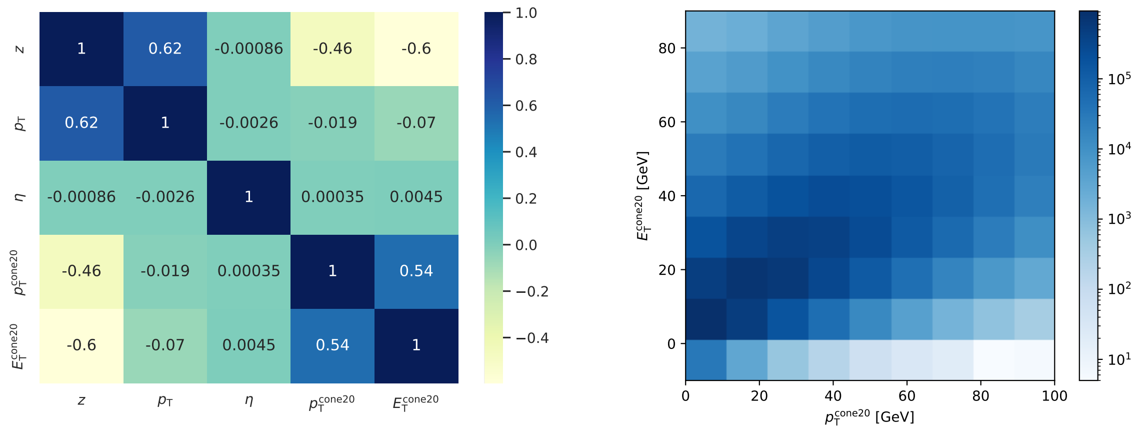

(a) (b)

Figure 4.6: Figure (a) depicts the Pearson correlation matrix of kinematic and isolation variables and (b) the two-dimensional plane of $E_{\mathrm{T}}^{\mathrm{cone20}}$ in dependence of $p_{\mathrm{T}}^{\mathrm{cone20}}$.

only be measured with a reduced presicion.
Additionally the correlation between z and the isolation variables $p_{\mathrm{T}}^{\mathrm{cone20}}$ or $E_{\mathrm{T}}^{\mathrm{cone20}}$ can be seen in the Appendix A.1.

4.4 Identification Variables

In the following, the impact of the fragmentation fraction z on particular SSVs is analysed. Subsequently, it is investigated whether the flavour of the parton that initiated the jet influences the probability that a non-prompt photon is reconstructed as a photon, which passes the tight identification criteria. Since the EM showers of converted and unconverted photons are induced by different particles, their SSV distributions are expected to be different, which is why they are studied separately.

The SSV $E_{\mathrm{ratio}} = \frac{E^{S1}_{\mathrm{max},1} - E^{S1}_{\mathrm{max},2}}{E^{S1}_{\mathrm{max},1} + E^{S1}_{\mathrm{max},2}}$ measures the difference between the first and second maximum of energy depositions in the cells in the strip layer. It provides discrimination between relatively narrow clusters, associated with single photon signatures, and broader, double-peaked topologies that are common for the two collimated photons from neutral pion decays. It is depicted in Figure 4.7 for unconverted photons on the left and converted photons on the right, categorised into all prompt photons and different z-intervals for non-prompt photons to compare the shape of the distributions of non-prompt photons with the shape of the signal distributions. Both figures show that these distributions become more signal-like for increasing fragmentation fractions. For the highest z-interval,

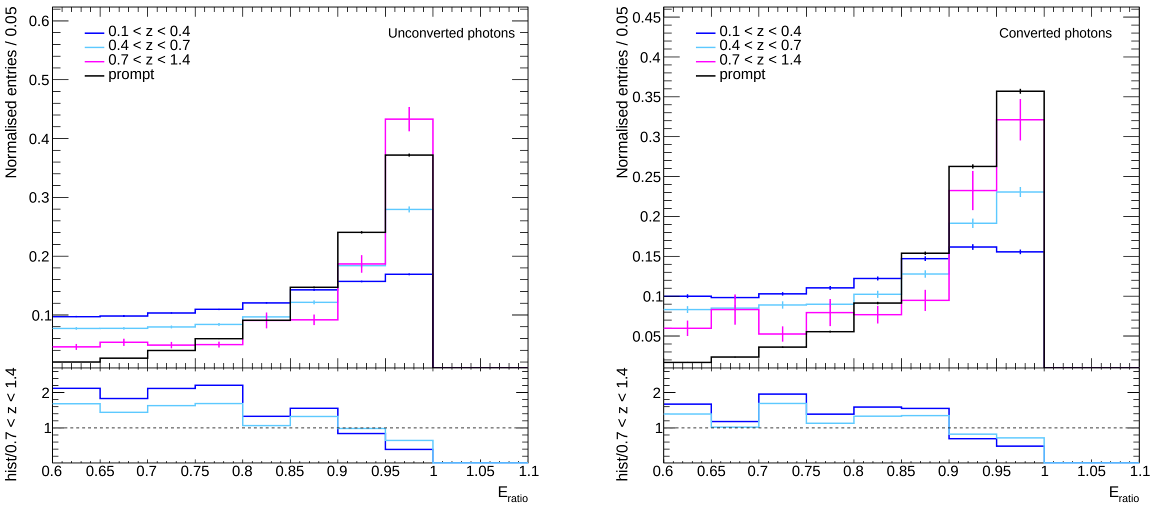

(a) (b)

Figure 4.7: Figure (a) shows the normalised distribution of the SSV E_{ratio} for unconverted photons and Figure (b) for converted photons. It is categorised into all prompt photons and different z-intervals for non-prompt photons.

the distributions are quite similar to the ones of prompt photons. This is expected because collimated photons with a high z tend to have very small opening angles so that the physical showers merge further and look more like the shower of a single photon.

Figure 4.8 shows the SSV $w_{\text{s tot}} = \sqrt{\frac{\sum E_i (i - i_{\text{max}})^2}{\sum E_i}}$, which describes the width of a shower in the first layer of the ECAL over 20 strips. A distinction is again made between all prompt photons and different z-intervals for non-prompt photons. It can be seen that the distributions of non-prompt photons become more signal-like for increasing z as well. In contrast to E_{ratio}, even the shape of the distribution with the highest z (ranging from 0.7 to 1.4) is quite different compared to the shape of the distribution of the prompt photons. Thus, it appears that the distance between the two shower maxima is not large enough to be separated by E_{ratio} with the given granularity of the first layer of the ATLAS ECAL, but the showers still tend to be wider than that of single photons with narrower showers. Therefore, $w_{\text{s tot}}$ provides better discrimination against non-prompt photons with a high z than E_{ratio}.

Distributions of additional SSVs are given in the Appendix A.2. In general, the picture remains similar to the variables discussed in more detail previously: non-prompt photons with higher z tend to lead to more signal-like SSV distributions.

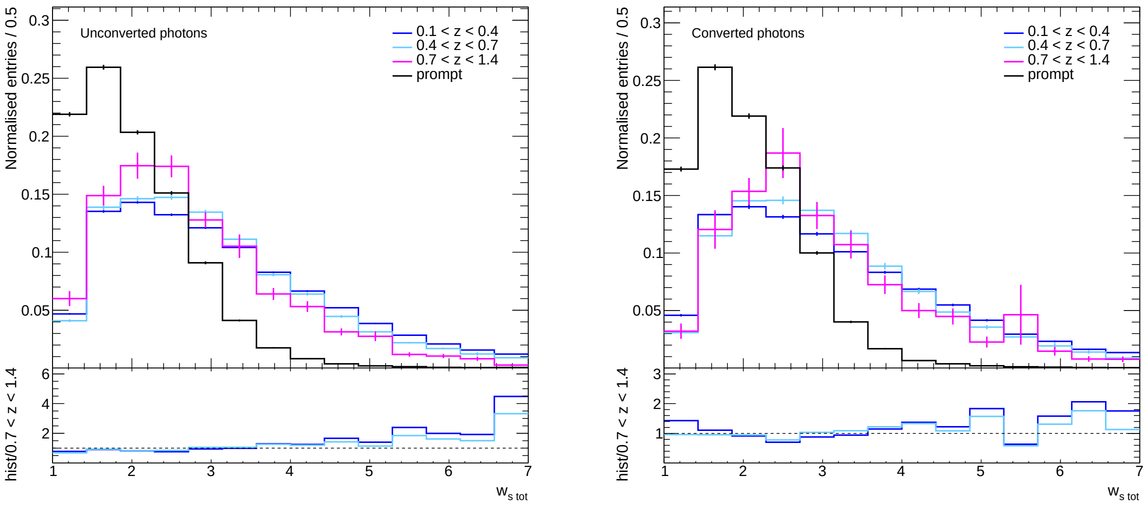

(a) **(b)**

Figure 4.8: Normalised distributions of the SSV $w_{\mathrm{s\,tot}}$ for unconverted (a) and converted (b) photons.

In Figure 4.9 the flavour of the closest jet [3] is depicted for loose, tight, and all non-prompt photons. In this figure, the numbers from one to five refer to down, up, strange, charm and bottom quarks and 21 represents gluon-induced jets [50]. The MC truth classifier [51] tries to assign what the particle really was (truth type) and what source it came from (truth origin). The truth origins and types of non-prompt photons for the different jet flavours are depicted in Figure 4.10. The codes for the truth type and origin will be explained later. For a complete overwiew, see Table A.1 for the truth type and A.2 for the truth origin in the appendix.

Figure 4.9 indicates that jets initiated by up and down quarks lead to tight photons with a larger probability while gluon-initiated jets lead to these with a smaller probability. This fits in with the observation that gluon jets have a higher charged particle multiplicity than quark jets for typical jet energies at the LHC [52,53]. Jets initiated by strange, charm and bottom quarks lead to photons passing the loose, tight or no identification WP with similar probabilities. Furthermore in Figure 4.10c, it can be seen that non-prompt photons in gluon-initiated jets more often originate from decays of strange and heavy flavour [4] mesons (truth origins 24-26) as well as baryons (truth origins 31-33)

[3]The jet itself has no flavour, but the parton from which it is created does. For the sake of simplicity, however, the expression "flavour of the jet" is used.

[4]Heavy flavour quarks are charm and bottom quarks. Top quarks are not included in this category because they are so massive that they mostly decay before they can form hadrons.

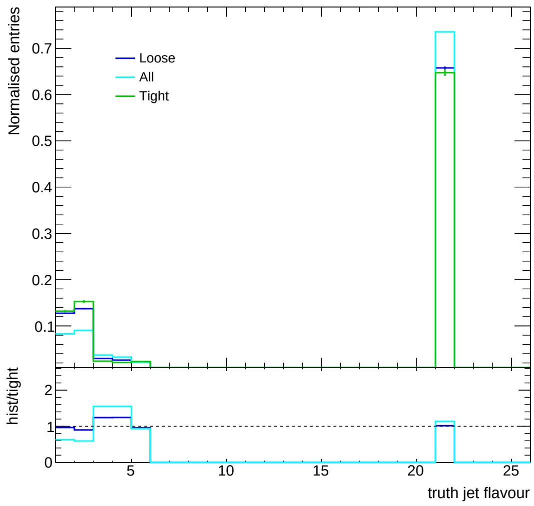

Figure 4.9: The truth flavour [50] of the closest jet to the leading photon for loose, tight, and all non-prompt photons. All histograms are normalised to unit area.

than in up and down jets. Moreover, in Figure 4.10b it can be seen that non-prompt leading photons in bottom and charm quark jets are more likely to be an electron from a hadron decay (truth type 3) than those from other jets. Consistent with this observation, Figure 4.10d shows that reconstructed photons in these jets receive contributions from electrons originating from hadron decays as well as decays of tau leptons (truth origin 9) that are generated in semileptonic decays (e.g. $B^- \to \tau^- \bar{\nu_\tau}$). This indicates that in heavy flavour jets a comparatively large proportion of the non-prompt reconstructed photons are actually electrons.

Due to the higher multiplicity of charged particles in gluon jets, the individual particles receive a smaller part of the momentum of the jet. This is consistent with the fact that gluons have softer fragmentation functions for pions compared to up and down quarks [54,55]. The reason that gluon jets more often contain photons from strange and heavy flavour hadron decays than up and down jets is that gluons, unlike up and down quarks, couple in *Leading Order* (LO) to strange and heavy flavour quarks. Furthermore, bottom jets tend to contain more electrons misreconstructed as photons than other jets, as noted before. This could explain why bottom jets, unlike gluon jets, lead to photons passing the loose, tight or no identification WP with a similar probability (see Figure 4.9), although bottom quark and gluon jets have a similar charged particle multiplicity [56]. Moreover, there is a larger number of reconstructed photons from π_0 decays (truth origin 42) in heavy flavour jets than in strange jets, as evident in Figure 4.10d. This probably results from hadron decay cascades in these jets as both b and c hadrons usually decay inside the detector.

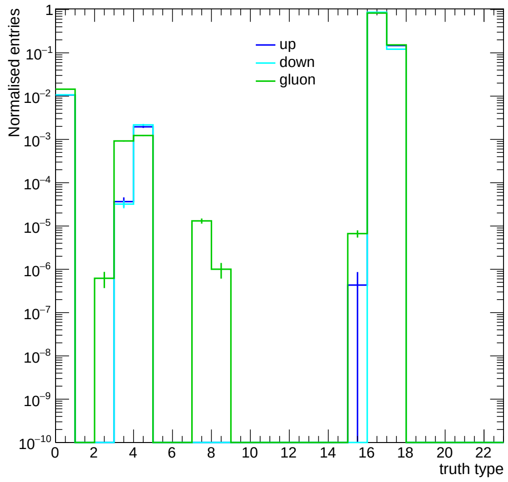

(a)

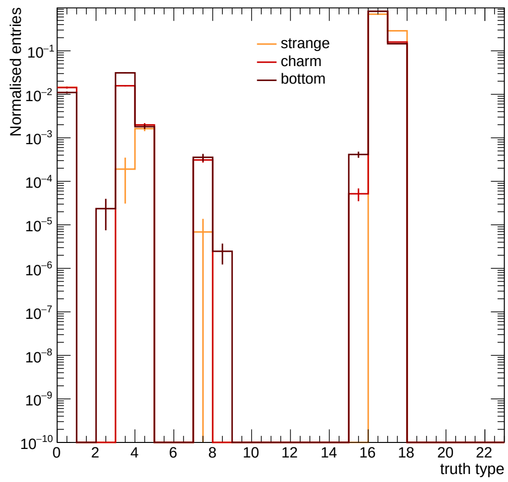

(b)

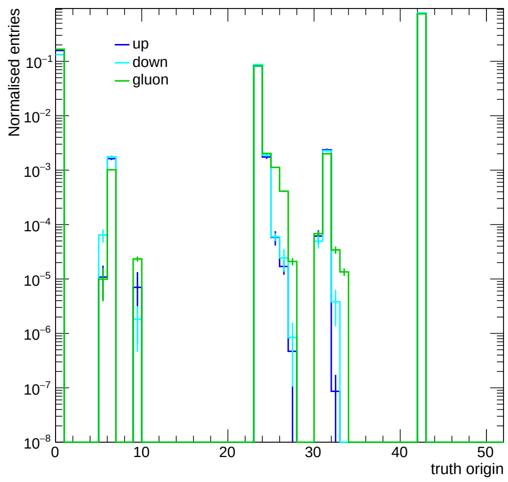

(c)

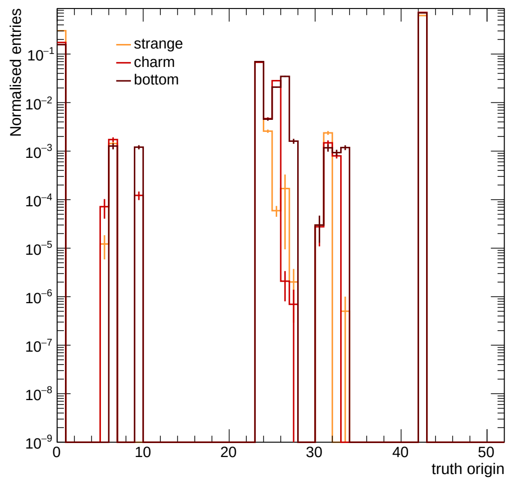

(d)

Figure 4.10: Normalised distributions of the truth type (a,b) and the truth origin (c,d) of the leading non-prompt photon for the different jet flavours.

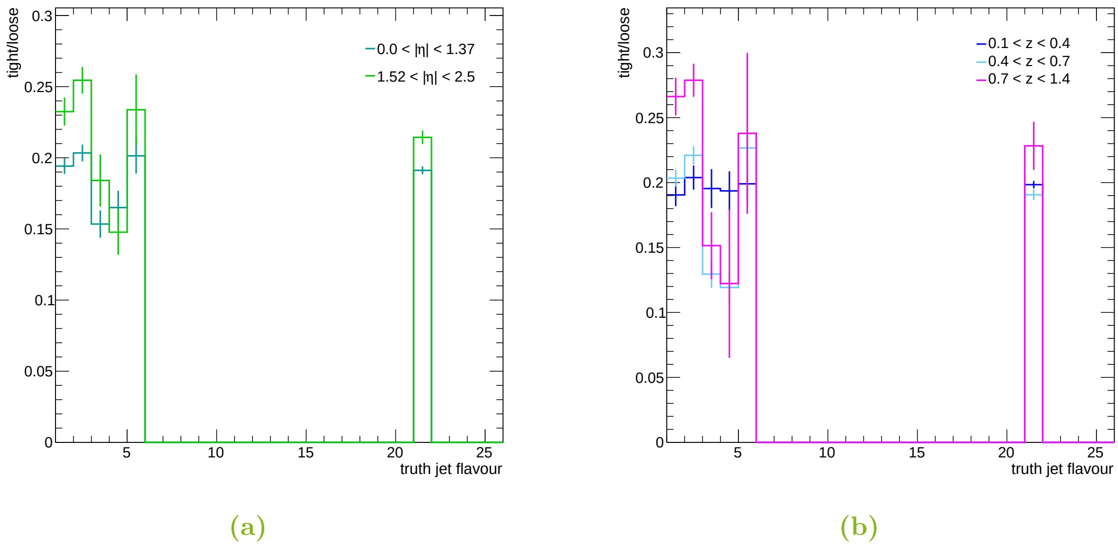

Figure 4.11: Ratio of the number of tight and loose photons for either different η-regions (a) or z-intervals (b) in dependence of the jet flavour.

In Figure 4.11, the ratio of the number of tight and loose photons for either different η-regions or z-intervals in dependence of the jet flavour are depicted. As can be observed in the left Figure 4.11a, non-prompt photons in the endcap section are more likely to pass the tight identification WP. The ECAL there provides a lower resolution than that of the barrel region. Therefore a similar signal efficiency of the tight identification WP in both regions results in a lower purity of a sample of tight photons in the endcap region compared to the barrel region. This could explain the observed difference. The lower resolution makes it more difficult to detect the double-peaked structure of collimated photons with a small opening angle. Furthermore, in Figure 4.11b it can be seen that the probability that a reconstructed photon in an up, down or gluon jet passes the tight identification WP tends to increase with z. This is consistent with the aforementioned observation that the probability that a non-prompt photon passes the tight identification WP increases with z. This is related to a decreasing opening angle between collimated photons, which mainly originate from π_0 meson decays. Since gluons, up and down quarks are the only partons that couple in LO to up and down quarks, which create pions, it is reasonable that the aforementioned trend is only clearly visible for these partons.

As an outlook for further investigations, the ratio of the number of tight and loose photons for converted and unconverted non-prompt photons in dependence of the jet flavour can be found in the Appendix A.1. As discussed in Section 4.1, thorough future studies of these numbers would require detailed analysis of the photon reconstruction algorithms at the ATLAS experiment.

4.5 Interpretation of the Results

In the previous sections, the samples were investigated regarding the conversion of photons and the impact of the jet flavour as well as the pseudorapidity. Furthermore, the correlation between the fragmentation fraction of the leading photon and the identification WPs, its isolation variables and its SSVs was studied.

It was observed that the distributions of converted and unconverted photons have different trends for their transverse momentum and their fragmentation fraction, which is surprising since these variables are strongly correlated. Furthermore, the conversion fraction is on average greater for non-prompt photons than for prompt photons, which is probably due to the smaller background rejection for prompt converted photons. In addition, the identification efficiency is slightly lower in the endcap region [37] since the endcap calorimeters are a bit coarser than those in the barrel region. This could explain why there is a greater fraction of tight to loose photons in this region. The probability of a leading non-prompt photon to pass the tight identification WP also increases with its fragmentation fraction, which is likely due to a decreasing opening angle between the collimated photons. A higher fragmentation fraction also leads to a lower average number of particles in the jet and thus to lower values of the isolation variables. Moreover, the distributions of the SSVs become in general more signal-like for an increasing z, although for some variables even the shape of the distribution with the highest z (ranging from 0.7 to 1.4) is quite distinct from the shape of the distribution of the prompt photons. Such variables, like $w_{\mathrm{s\,tot}}$, are well suited for separating prompt and non-prompt photons even for high z.

The flavour of the jet has an impact on the properties of the non-prompt photons as well. The probability that a photon passes the tight identification WP is higher for up and down jets and lower for gluon jets. This is because gluons have softer fragmentation functions for pions than up and down quarks and, corresponding to this, a greater multiplicity of charged particles in the jet. This supports the conclusion made earlier about the relationship between the fragmentation fraction and the number of particles in a jet. Furthermore, it was observed that charm and bottom jets tend to contain more electrons that were incorrectly reconstructed as photons than other jets. This explains why the probabilities of passing the loose and tight identification WPs of reconstructed photons in bottom jets are between those of gluon jets and light quark jets although they have a comparable charged particle multiplicity to gluon jets. Hence it could be useful for analyses with several bottom jets and prompt photons in the final state to require minimum angular distances between b-tagged jets and photons or to use dedicated electron veto algorithms on top of standard overlap removal techniques as implemented in, for example, [57].

5 Conclusions

Since many interesting processes studied in hadron-hadron collisions at the ATLAS experiment at the LHC suffer from background contributions of non-prompt photons, it is essential to have detailed knowledge about their properties. A large contribution of non-prompt photons arises from decays of neutral pions in jets to two collimated photons. For the studies, MC samples were analysed to identify properties of these non-prompt photons that are useful to separate them from prompt photons. The samples correspond to the data taking conditions of 2017, meaning a centre-of-mass energy of 13 TeV and a mean number of interactions per crossing of $\langle \mu \rangle = 37.8$. These samples were analysed regarding the impact of the conversion status, the jet flavour and the pseudorapidity. Moreover, the correlation between the fragmentation fraction z of the leading photon, its identification status, its isolation variables and its SSVs, that describe the evolution of its electromagnetic shower in the ECAL, is studied.

Since converted and unconverted photons exhibit differences at reconstruction level, the influence of the conversion status on different variables is particularly important for improving the separation of prompt and non-prompt photons. This should be investigated more deeply in further studies.

It was established that the probability of a non-prompt photon to pass the tight identification WP and its isolation increase with its fragmentation fraction. Furthermore, an increasing fraction leads to more signal-like SSVs. This phenomenon can be explained by a smaller opening angle between two collimated photons and less contaminated shower shapes. Therefore, it could be an option to keep jets close to reconstructed photons and parametrise the photon identification criteria in z for photons with nearby jets.

It was also determined that strange, charm and bottom jets tend to contain more electrons, which were incorrectly reconstructed as photons. Hence, it could be beneficial to apply minimum angular distances between jets and photons or special electron vetos.

In comparison to the data-taking period from 2015 to 2018, the effects of pile-up will become increasingly relevant in Run-3 due to the higher instantenous luminosity. This also justifies the choice of 2017 for the data-taking conditions for the Monte Carlo samples, because $\langle \mu \rangle$ was highest in that year of Run-2. Furthermore, the centre-of-mass energy is not increased substantially and it is not expected that the photon reconstruction algorithms change to great extent in Run-3. Thus the studies can be applied to Run-3 conditions with comparatively minor extrapolations.

Lastly, the studies should be repeated with samples from other MC generators to assess the systematic differences between them and their impact on the properties of non-prompt photons in simulation.

A Appendix

A.1 Additional Material regarding Kinematics, Isolation and Conversion Status

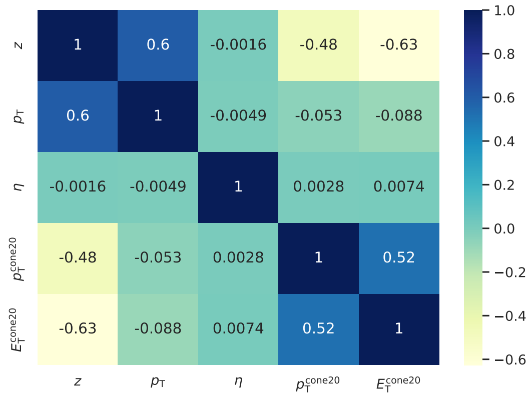

Figure A.1: The Spearman correlation matrix of kinematical and isolation variables of non-prompt photons.

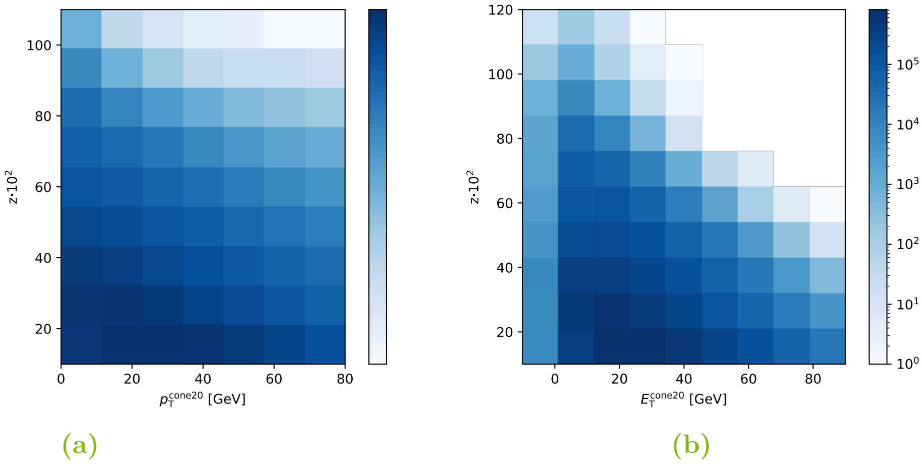

Figure A.2: The two-dimensional plane of z in dependence of $p_{\mathrm{T}}^{\mathrm{cone20}}$ (a) or $E_{\mathrm{T}}^{\mathrm{cone20}}$ (b).

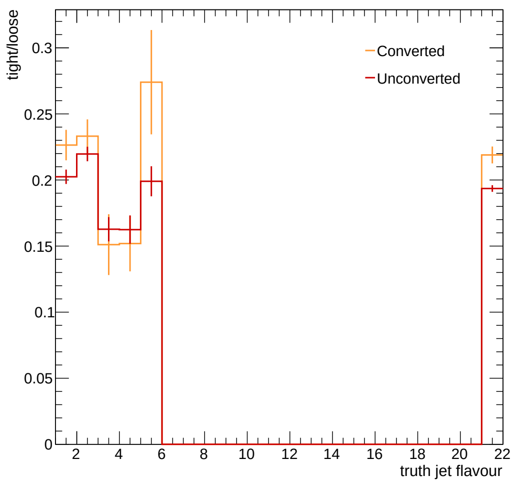

Figure A.3: The normalised distributions of the ratio of the number of tight and loose photons for converted and unconverted non-prompt photons in dependence of the flavour of the closest jet.

A.2 Additional Shower Shape Variables

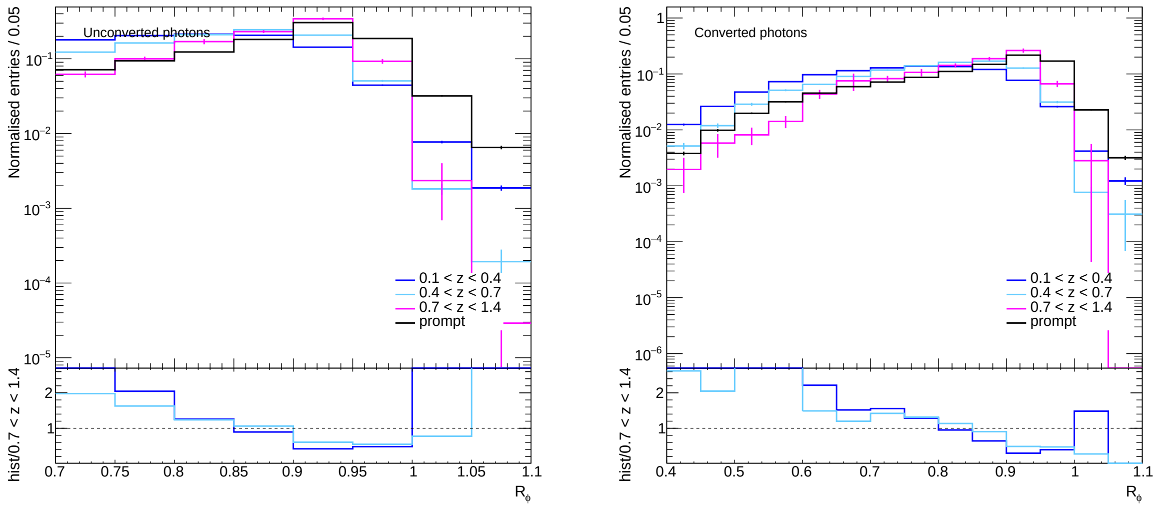

(a) **(b)**

Figure A.4: The normalised distributions of the shower shape variable R_ϕ for unconverted (a) and converted (b) photons.

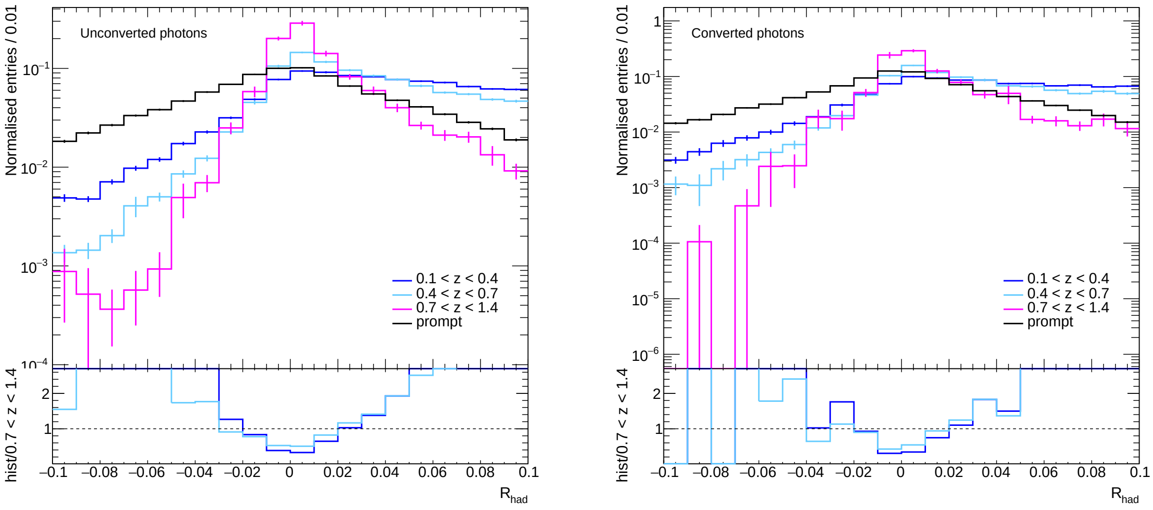

(a) (b)

Figure A.5: The normalised distributions of the shower shape variable R_{had} for unconverted (a) and converted (b) photons.

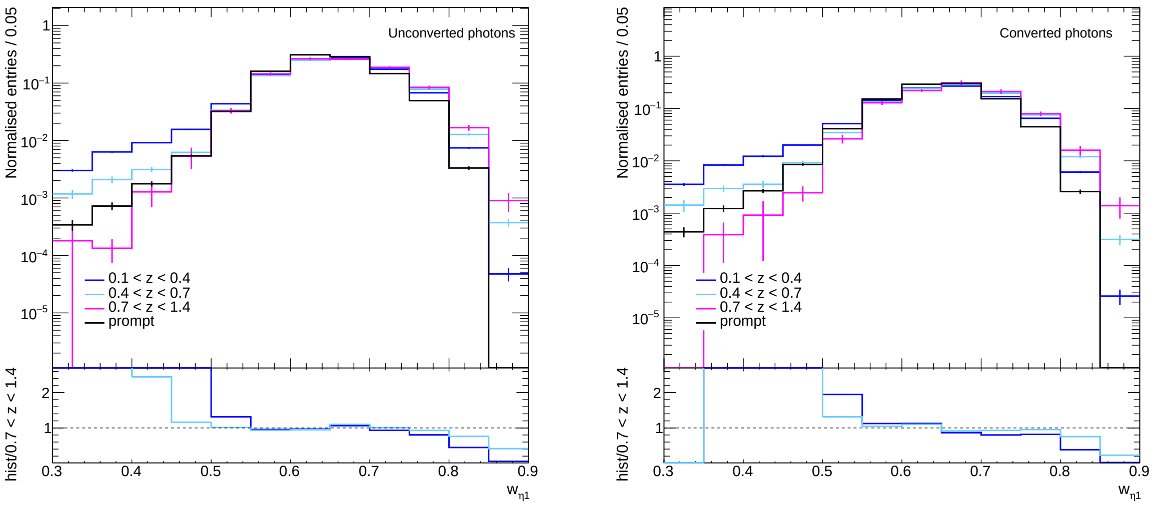

(a) (b)

Figure A.6: The normalised distributions of the shower shape variable $w_{\eta 1}$ for unconverted (a) and converted (b) photons.

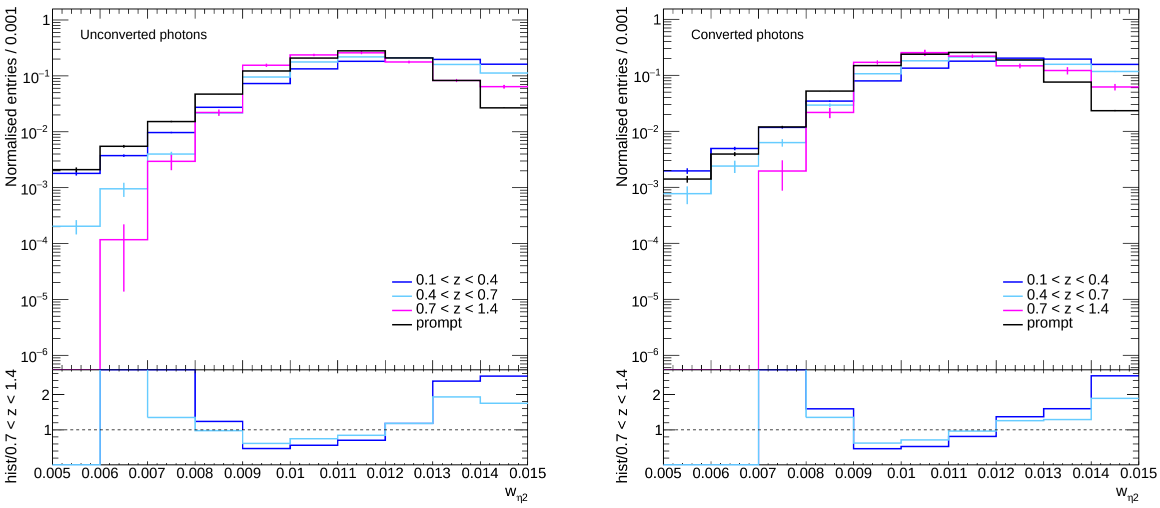

(a) **(b)**

Figure A.7: The normalised distributions of the shower shape variable $w_{\eta 2}$ for unconverted (a) and converted (b) photons.

A.3 Monte Carlo Truth Classifier

Table A.1: Definition of the particle truth type of the MC truth classifier [51].

Particle Type	Number	Particle Type	Number
Unknown	0	NonPrimary	20
UnknownElectron	1	GenParticle	21
IsoElectron	2	SUSYParticle	22
NonIsoElectron	3	BBbarMesonPart	23
BkgElectron	4	BottomMesonPart	24
UnknownMuon	5	CCbarMesonPart	25
IsoMuon	6	CharmedMesonPart	26
NonIsoMuon	7	BottomBaryonPart	27
BkgMuon	8	CharmedBaryonPart	28
UnknownTau	9	StrangeBaryonPart	29
IsoTau	10	LightBaryonPart	30
NonIsoTau	11	StrangeMesonPart	31
BkgTau	12	LightMesonPart	32
UnknownPhoton	13	BJet	33
IsoPhoton	14	CJet	34
NonIsoPhoton	15	LJet	35
BkgPhoton	16	GJet	36
Hadron	17	TauJet	37
Neutrino	18	UnknownJet	38
NuclFrag	19	OtherBSMParticle	39

Table A.2: Definition of the particle truth origin of the MC truth classifier [51].

Particle Origin	Number	Particle Origin	Number
NonDefined	0	StrangeMeson	24
SingleElec	1	CharmedMeson	25
SingleMuon	2	BottomMeson	26
SinglePhot	3	CCbarMeson	27
SingleTau	4	JPsi	28
PhotonConv	5	BBbarMeson	29
DalitzDec	6	LightBaryon	30
ElMagProc	7	StrangeBaryon	31
Mu	8	CharmedBaryon	32
TauLep	9	BottomBaryon	33
top	10	PionDecay	34
QuarkWeakDec	11	KaonDecay	35
WBoson	12	BremPhot	36
ZBoson	13	PromptPhot	37
Higgs	14	UndrPhot	38
HiggsMSSM	15	ISRPhot	39
HeavyBoson	16	FSRPhot	40
WBosonLRSM	17	NucReact	41
NuREle	18	PiZero	42
NuRMu	19	DiBoson	43
NuRTau	20	ZorHeavyBoson	44
LQ	21	QCD	45
SUSY	22	OtherBSM	46
LightMeson	23	MultiBoson	47

Bibliography

[1] S. L. Glashow, *Partial Symmetries of Weak Interactions*, Nucl. Phys. **22** (1961) 579.

[2] S. Weinberg, *A Model of Leptons*, Phys. Rev. Lett. **19** (1967) 1264.

[3] A. Salam, *Weak and Electromagnetic Interactions*, Conf. Proc. C **680519** (1968) 367.

[4] G. 't Hooft and M. J. G. Veltman, *Regularization and Renormalization of Gauge Fields*, Nucl. Phys. B **44** (1972) 189.

[5] D. Galbraith and C. Burgard, *Example: Standard model of physics*, 2016, URL: `https://texample.net/tikz/examples/model-physics/` (visited on 06/22/2022).

[6] F. Englert and R. Brout, *Broken Symmetry and the Mass of Gauge Vector Mesons*, Phys. Rev. Lett. **13** (1964) 321.

[7] P. W. Higgs, *Broken symmetries, massless particles and gauge fields*, Phys. Lett. **12** (1964) 132.

[8] P. W. Higgs, *Broken Symmetries and the Masses of Gauge Bosons*, Phys. Rev. Lett. **13** (1964) 508.

[9] G. S. Guralnik, C. R. Hagen, and T. W. B. Kibble, *Global Conservation Laws and Massless Particles*, Phys. Rev. Lett. **13** (1964) 585.

[10] P. W. Higgs, *Spontaneous Symmetry Breakdown without Massless Bosons*, Phys. Rev. **145** (1966) 1156.

[11] T. W. B. Kibble, *Symmetry breaking in non-Abelian gauge theories*, Phys. Rev. **155** (1967) 1554.

[12] D. Oriti et al., *Approaches to Quantum Gravity*, 1. edition, Cambridge University Press, 2009.

[13] L. Canetti, M. Drewes, and M. Shaposhnikov, *Matter and Antimatter in the Universe*, New J. Phys. **14** (2012) 095012.

[14] G. Bertone, D. Hooper, and J. Silk, *Particle dark matter: Evidence, candidates and constraints*, Phys. Rept. **405** (2005) 279.

[15] M. Klasen and F. König, *New information on photon fragmentation functions*, Eur. Phys. J. C **74** (2014) 3009.

[16] T. Kaufmann, A. Mukherjee, and W. Vogelsang, *Recent developments on parton-to-photon fragmentation functions*, CERN Proc. **1** (2018) 211.

[17] P. A. Zyla et al., *The Review of Paricle Physics, Chap. 19. Fragmentation Functions in e^+e^-, ep, and pp Collisions*, Prog. Theor. Exp. Phys. 2020 (2020) 083C01, ed. by O. Biebel et al.

[18] ATLAS Collaboration, *Observation of a new particle in the search for the Standard Model Higgs boson with the ATLAS detector at the LHC*, Phys. Lett. B **716** (2012) 1.

[19] CMS collaboration, *Observation of a New Boson at a Mass of 125 GeV with the CMS Experiment at the LHC*, Phys. Lett. B **716** (2012) 30.

[20] ATLAS collaboration, *Evidence for electroweak production of two jets in association with a $Z\gamma$ pair in pp collisions at $\sqrt{s} = 13$ TeV with the ATLAS detector*, Phys. Lett. B **803** (2020) 135341.

[21] CMS Collaboration, *Measurement of the electroweak production of $Z\gamma$ and two jets in proton-proton collisions at $\sqrt{s} = 13$ TeV and constraints on anomalous quartic gauge couplings*, Phys. Rev. D **104** (2021) 072001.

[22] ATLAS collaboration, *Measurement of the production cross section of pairs of isolated photons in pp collisions at 13 TeV with the ATLAS detector*, JHEP **11** (2021) 169.

[23] CMS collaboration, *Measurements of the differential cross sections of the production of Z + jets and γ + jets and of Z boson emission collinear with a jet in pp collisions at $\sqrt{s}$ = 13 TeV*, JHEP **05** (2021) 285.

[24] ATLAS collaboration, *Measurements of inclusive and differential cross-sections of combined $t\bar{t}\gamma$ and $tW\gamma$ production in the $e\mu$ channel at 13 TeV with the ATLAS detector*, JHEP **09** (2020) 049.

[25] ATLAS collaboration, *Observation of single-top-quark production in association with a photon at the ATLAS detector*, (2022), ATLAS-CONF-2022-013.

[26] ATLAS collaboration, *Search for flavour-changing neutral-current couplings between the top quark and the photon with the ATLAS detector at $\sqrt{s} = 13$ TeV*, (2022), URL: https://arxiv.org/abs/2205.02537.

[27] CMS collaboration, *Search for new physics in final states with a single photon and missing transverse momentum in proton-proton collisions at $\sqrt{s}$ = 13 TeV*, JHEP **02** (2019) 074.

[28] L. Evans and P. Bryant (Eds.), *LHC Machine*, JINST **3** (2008) 08001.

[29] ATLAS Collaboration, *The ATLAS Experiment at the CERN Large Hadron Collider*, JINST **3** (2008) 08003.

[30] CMS Collaboration, *The CMS Experiment at the CERN LHC*, JINST **3** (2008) 08004.

[31] LHCb Collaboration, *The LHCb Detector at the LHC*, JINST **3** (2008) 08005.

[32] ALICE Collaboration, *The ALICE experiment at the CERN LHC*, JINST **3** (2008) 08002.

[33] ATLAS Collaboration, *ATLAS data quality operations and performance for 2015–2018 data-taking*, JINST **15** (2020) 04003.

[34] CERN organisation, *Longer term LHC schedule*, 2022, URL: `https://lhc-commissioning.web.cern.ch/schedule/LHC-long-term.htm` (visited on 07/06/2022).

[35] ATLAS collaboration, *Electron and photon performance measurements with the ATLAS detector using the 2015–2017 LHC proton-proton collision data*, JINST **14** (2019) 12006.

[36] N. Buatthaisong, *Electron/Photon Ambiguity Resolution Using Neural networks For ATLAS Experiment*, (2019), Summer Student Project Report, URL: `https://www.desy.de/f/students/2019/reports/nutthawara.buatthaisong.pdf`.

[37] ATLAS collaboration, *Measurement of the photon identification efficiencies with the ATLAS detector using LHC Run 2 data collected in 2015 and 2016*, Eur. Phys. J. C **79** (2019) 205.

[38] ATLAS collaboration, *Measurement of the photon identification efficiencies with the ATLAS detector using LHC Run-1 data*, Eur. Phys. J. C **76** (2016) 666.

[39] J. C. Saxon, *Discovery of the Higgs Boson, Measurements of its Production, and a Search for Higgs Boson Pair Production*, (2014), PhD thesis.

[40] M. Cacciari, G. P. Salam, and G. Soyez, *The anti-k_t jet clustering algorithm*, JHEP **4** (2008) 63.

[41] M. Cacciari, G. P. Salam, and G. Soyez, *FastJet User Manual*, Eur. Phys. J. C **72** (2012) 1896.

[42] ATLAS collaboration, *Jet reconstruction and performance using particle flow with the ATLAS Detector*, Eur. Phys. J. C **77** (2017) 466.

[43] ATLAS collaboration, *Performance of pile-up mitigation techniques for jets in pp collisions at $\sqrt{s} = 8$ TeV using the ATLAS detector*, Eur. Phys. J. C **76** (2016) 581.

[44] T. Sjöstrand, S. Mrenna, and P. Z. Skands, *A Brief Introduction to PYTHIA 8.1*, Comput. Phys. Commun. **178** (2008) 852.

[45] ATLAS collaboration, *The ATLAS Simulation Infrastructure*, Eur. Phys. J. C **70** (2010) 823.

[46] S. Agostinelli et al., *Geant4—a simulation toolkit*, Nucl. Instrum. Meth. A **506** (2003) 250.

[47] ATLAS collaboration, *ATLAS Experiment - Public Results, LuminosityPublicResultsRun2*, (2022), URL: `https://twiki.cern.ch/twiki/bin/view/AtlasPublic/LuminosityPublicResultsRun2`.

[48] L. P. Dominguez, *Studies of photon isolation in a large-pileup environment and search for axion-like particles decaying into two photons with the ATLAS detector at the LHC*, PhD thesis, 2021.

[49] L. C. Maximon, *Simple analytic expressions for the total Born approximation cross section for pair production in a Coulomb field*, J. Res. Nat. Bur. Stand. - Math. Sci. **72B** (1968) 79.

[50] P. A. Zyla et al., *The Review of Paricle Physics, Chap. 45. Monte Carlo Particle Numbering Scheme*, Prog. Theor. Exp. Phys. 2020 (2020) 083C01.

[51] ATLAS Collaboration, *Athena*, version 22.0.1, Zenodo (2010), URL: `https://gitlab.cern.ch/atlas/athena/blob/21.2/PhysicsAnalysis/MCTruthClassifier/MCTruthClassifier/MCTruthClassifierDefs.h`.

[52] OPAL collaboration, *A direct observation of quark-gluon jet differences at LEP*, Phys. Lett. B **265** (1991) 462.

[53] OPAL collaboration, *Experimental properties of gluon and quark jets from a point source*, Eur. Phys. J. C **11** (1999) 217.

[54] D. de Florian, R. Sassot, and M. Stratmann, *Global analysis of fragmentation functions for protons and charged hadrons*, Phys. Rev. D **76** (2007) 074033.

[55] D. de Florian et al., *Parton-to-Pion Fragmentation Reloaded*, Phys. Rev. D **91** (2015) 014035.

[56] OPAL collaboration, *A Comparison of b and (uds) quark jets to gluon jets*, Z. Phys. C **69** (1996) 543.

[57] ATLAS collaboration, *Search for Higgs boson pair production in the two bottom quarks plus two photons final state in pp collisions at $\sqrt{s} = 13$ TeV with the ATLAS detector*, (2021), URL: `https://arxiv.org/abs/2112.11876`.

Eidesstattliche Versicherung

(Affidavit)

Deponte, Chiara

Name, Vorname
(surname, first name)

219449

Matrikelnummer
(student ID number)

■ Bachelorarbeit
(Bachelor's thesis)

☐ Masterarbeit
(Master's thesis)

Titel
(Title)

Studies on the properties of non-prompt photons at the ATLAS experiment

Ich versichere hiermit an Eides statt, dass ich die vorliegende Abschlussarbeit mit dem oben genannten Titel selbstständig und ohne unzulässige fremde Hilfe erbracht habe. Ich habe keine anderen als die angegebenen Quellen und Hilfsmittel benutzt sowie wörtliche und sinngemäße Zitate kenntlich gemacht. Die Arbeit hat in gleicher oder ähnlicher Form noch keiner Prüfungsbehörde vorgelegen.

I declare in lieu of oath that I have completed the present thesis with the above-mentioned title independently and without any unauthorized assistance. I have not used any other sources or aids than the ones listed and have documented quotations and paraphrases as such. The thesis in its current or similar version has not been submitted to an auditing institution before.

Dortmund, 15.07.2022

Ort, Datum
(place, date)

Chiara Deponte

Unterschrift
(signature)

Belehrung:
Wer vorsätzlich gegen eine die Täuschung über Prüfungsleistungen betreffende Regelung einer Hochschulprüfungsordnung verstößt, handelt ordnungswidrig. Die Ordnungswidrigkeit kann mit einer Geldbuße von bis zu 50.000,00 € geahndet werden. Zuständige Verwaltungsbehörde für die Verfolgung und Ahndung von Ordnungswidrigkeiten ist der Kanzler/die Kanzlerin der Technischen Universität Dortmund. Im Falle eines mehrfachen oder sonstigen schwerwiegenden Täuschungsversuches kann der Prüfling zudem exmatrikuliert werden. (§ 63 Abs. 5 Hochschulgesetz - HG -).

Die Abgabe einer falschen Versicherung an Eides statt wird mit Freiheitsstrafe bis zu 3 Jahren oder mit Geldstrafe bestraft.

Die Technische Universität Dortmund wird ggf. elektronische Vergleichswerkzeuge (wie z.B. die Software „turnitin") zur Überprüfung von Ordnungswidrigkeiten in Prüfungsverfahren nutzen.

Die oben stehende Belehrung habe ich zur Kenntnis genommen:

Official notification:
Any person who intentionally breaches any regulation of university examination regulations relating to deception in examination performance is acting improperly. This offense can be punished with a fine of up to EUR 50,000.00. The competent administrative authority for the pursuit and prosecution of offenses of this type is the Chancellor of TU Dortmund University. In the case of multiple or other serious attempts at deception, the examinee can also be unenrolled, Section 63 (5) North Rhine-Westphalia Higher Education Act (*Hochschulgesetz, HG*).

The submission of a false affidavit will be punished with a prison sentence of up to three years or a fine.

As may be necessary, TU Dortmund University will make use of electronic plagiarism-prevention tools (e.g. the "turnitin" service) in order to monitor violations during the examination procedures.

I have taken note of the above official notification:*

Dortmund, 15.07.2022

Ort, Datum
(place, date)

Chiara Deponte

Unterschrift
(signature)

***Please be aware that solely the German version of the affidavit ("Eidesstattliche Versicherung") for the Bachelor's/ Master's thesis is the official and legally binding version.**